Strengthened relationship between sea ice in East Siberian Sea and midsummer rainfall in Northeast China

Tingting Han (hantt08@126.com)
Nanjing University of Information Science and Technology https://orcid.org/0000-0002-4749-3792
Guowa Tang
Nanjing University of Information Science and Technology
Botao Zhou
Nanjing University of Information Science and Technology
Xin Hao
Nanjing University of Information Science and Technology
Shangfeng Li
Institute of Meteorology Sciences of Jilin Province

Research Article

Keywords: midsummer rainfall in Northeast China, Arctic sea ice, interdecadal change, interannual variability

Posted Date: June 22nd, 2022

DOI: https://doi.org/10.21203/rs.3.rs-1689151/v1

Abstract

Arctic sea ice displays the high rates of decay during summer-autumn. Previous studies have revealed the impact of autumn Arctic sea ice on local and remote atmospheric circulation. Few attentions have been paid on the relationship between summer Arctic sea ice and climate variation at Eurasia. This study identifies a strengthened relationship between midsummer rainfall at Northeast China (NEC) and simultaneous sea ice area (SIA) in East Siberian Sea after the 1990s. The NEC's rainfall shows a significant positive correlation with the SIA during 1994 – 2016, whereas the relationship is insignificant during 1961 – 1983. The strengthening of the relationship is attributed to the western elongation of background circulation at the North Pacific and the increased interannual variability of the SIA after the 1990s. The former facilitates the western extension of the SIAI-associated circulation over the Central North Pacific. The latter induces larger amplitudes of sea ice and surface heat fluxes in situ, and then it leads to stronger meridional temperature gradient anomalies and intensified interaction between synoptic-scale eddies and mean flow over the North Pacific. These conditions jointly contribute to stronger and western elongation of circulation over the Central North Pacific during 1994 – 2016. Accordingly, the SIA has an intimate connection with NEC's rainfall though the modulation of moisture transport and vertical movement.

1. Introduction

Northeast China (NEC) is among the regions in China that are most affected by climate change (Zuo et al. 2004). Climate variation in this region, especially rainfall variability, exerts substantial impacts on crop yield and people's lives (Zhou et al. 2013; Zhou and Wang 2015). However, less attention has been paid to rainfall variations in NEC than North China, the Yangtze River valley and South China. Therefore, it is essential to investigate the mechanisms governing the variability and spatial distribution of rainfall in this region.

It is acknowledged that summer rainfall accounts for a majority of the total annual rainfall in NEC (Liang et al. 2011). Some efforts have been devoted to identifying the factors and mechanisms that govern the annual and decadal variations in summer rainfall (Zhu 2011; Gao 2014a). For example, the East Asian summer monsoon circulation is linked with the moisture transport associated with NEC's rainfall (Sun et al. 2017). Using the averaged 850-hPa vorticity within NEC, Han et al. (2015) defined a Northeast Asia summer monsoon index (NEASM) and revealed that the weakened NEASM after the late 1990s led to the recent decrease in summer rainfall. Generally, a strong cold vortex is accompanied by intensified convective anomalies and lead to a heavy rainfall event at NEC (Li et al. 2016). Gao et al. (2014b) proposed that the late spring rainfall anomaly in the Huang-Huai region causes anomalous local soil moisture and contributes to the following summer general circulation and rainfall anomalies at NEC. After the late 1980s, the sea surface temperature (SST) anomalies in the tropical Indian Ocean could excite an effective Rossby wave source at the Mediterranean and trigger Rossby wave at the midlatitude Eurasia, which further affects circulation anomalies at East Asia and NEC's rainfall (Han et al. 2018).

From the above discussion, it is clear that previous studies have mainly focused on the summer mean rainfall at NEC. Nevertheless, Shen et al. (2011) stated that the interannual variation in NEC's rainfall is predominantly influenced by cold vortex activity during early summer and by the East Asian summer monsoon circulation in midsummer. Moreover, analyses of observations and numerical simulations have indicated that the tropical Indian Ocean SST has had a stronger influence on midsummer rainfall in NEC since the late 1990s (Han et al. 2017), whereas the influence on early summer rainfall did not become significant until the late 1980s (Han et al. 2018). Therefore, separate analyses should be performed on rainfall variations during early summer and midsummer. This study focuses on midsummer rainfall in NEC because the amounts and interannual variability of rainfall is greater in midsummer than other seasons (Fig. S1).

In recent decades, increasing attention has been paid to the changes in Arctic sea ice due to mounting evidence that Arctic sea ice loss can influence local and remote weather and climate by modulating surface albedo and the exchange of radiation, heat and momentum between the ocean and the atmosphere (Alexander et al. 2004; Dethlof et al. 2006; Vihma 2014; Screen et al. 2018). Herman and Johnson (1978) initially noted the impact of winter Arctic sea ice cover on atmospheric circulation, even in subtropical regions. The impact of Arctic sea ice loss on the Eurasian winter climate has been demonstrated by substantial studies (Honda et al. 2009; Tang et al. 2013; Gao et al. 2015). For example, the recent decline in Arctic sea ice has made critical contributions to recent cold and snowy winters over Eurasia and North America (Liu et al. 2012; Mori et al. 2014; Cohen et al. 2019). Although some modeling studies imply a weak influence of Arctic sea ice loss on the winter climate variation at the midlatitudes (e.g., Ogawa et al. 2018; Blackport et al. 2019), the linkage between recent Arctic sea ice loss and the frequency and persistence of winter cold events over Asia has been documented by most recent studies (Luo et al. 2019; Francis et al. 2020). The controversy suggests the atmospheric circulation and climate change response to sea ice reduction could vary regionally and seasonally. Therefore, more efforts should be devoted the role of Arctic sea ice in Northern Hemisphere climate variation and the related mechanisms.

Moreover, recent summers have observed considerable decreases in the Arctic sea ice cover (Dai et al. 2019). The Arctic sea ice changes could affect atmospheric circulation and climate change during summer through three modulating the intensity of storm tracks (Petrie et al. 2015), meridional jet shifts (Zappa et al. 2018), and the amplitude of wave trains (Screen 2013). Some studies address the linkage of previous Arctic sea ice and summer rainfall in East Asia (Wu et al. 2009; Guo et al. 2014; Liu et al. 2020). Zhao et al. (2004) showed that a reduced Arctic sea ice extent could induce enhanced summer monsoon rainfall in southeastern China by background atmospheric circulation changes and stationary wave dynamics. NEC is located at mid-to-high latitudes in the Northern Hemisphere. The Arctic sea ice anomaly is also a predominant contributor to summer climate variations over NEC. Zhou and Wang (2014) illustrated the effect of late winter sea ice in the Bering Sea on rainfall amounts and diurnal temperature variation in NEC and further on maize and rice production. Li et al. (2018) suggested that spring sea ice anomaly over the Barents Sea modulates summer hot drought events in NEC on an interannual timescale.

From the above discussion, most previous studies have focused on the impact of autumn Arctic sea ice on the following climate variability and weather events at the Northern Hemisphere. Additionally, the Arctic sea ice concentration has declined considerably since the late 1970s, with relatively large reductions during summer-autumn (Dai et al. 2019). Wang and He (2015) determined that the summertime Arctic sea ice anomaly contributed to the severe drought in Northeast Asia in 2014. Motived by the above studies, the present study aims to investigate whether there exists a significant relationship between summer Arctic sea ice and NEC's rainfall. If does, whether the relationship is stable or not. And the related mechanism is also explored.

The rest of this paper is organized as follows. Section 2 introduces the datasets and methods used in the present study. Details of the relationship between sea ice and the NEC's rainfall and the possible underlying mechanisms are described in Section 3. Finally, brief conclusion and discussion are presented in Section 4.

2. Data And Methods

The monthly global atmospheric reanalysis dataset is extracted from the National Center for Environment Prediction & National Center for Atmospheric Research (NCEP/NCAR) (Kalnay et al. 1996). The variables used in this study include sea level pressure (SLP), geopotential height, three-dimensional winds, air temperature, and specific humidity. The daily mean wind data from the NCEP/NCAR are used to calculate the extended Eliassen-Palm (EP) flux. The atmospheric data from the NCEP/NCAR all have a resolution of 2.5° × 2.5°. This study also employs daily upward longwave radiation flux and sensible and latent heat flux data from the NCEP/NCAR on 192×94 Gaussian grids. The monthly sea ice concentration data from 1870 – 2016, with a 1.0° × 1.0° grid, are provided by the Met Office Hadley Centre (Rayner et al. 2003).

An advanced daily rainfall observation dataset (i.e., CN05.1) is used in the present study (Wu and Gao 2013). This dataset, which has a high resolution of 0.25° × 0.25°, is constructed based on an interpolation from over 2400 meteorological stations in China. NEC is defined as the region north of 38°N and east of 115°E in China and includes Heilongjiang Province, Jilin Province, Liaoning Province, and East four Leagues of Inner Mongolia. At NEC, the midsummer rainfall features distinct regional characteristics, including spatial homogeneity and south-north reversal pattern (Han et al. 2019). Specifically, the leading empirical orthogonal function (EOF) mode behaves homogenously over NEC (Fig. 1a), and the corresponding time series (shorted as PC1) exhibits strong covariance with the rainfall averaged within NEC (R = 0.97 during 1961–2016). Therefore, the leading EOF mode and the normalized PC1 are used to represent the spatial and temporal features of NEC's rainfall in this study, respectively.

In the present study, the extended EP flux is used to qualitatively determine the dynamical interactions between the synoptic□scale eddy activity and mean flow (Trenberth 1986). The horizontal extended EP flux is defined as follows, following Trenberth (1986).

$$E_u = \left[\frac{1}{2}\left(\bar{v}^2 - \bar{u}^2\right)\vec{i}, -\bar{u}\bar{v}\vec{j}\right] \times \cos\phi$$

1

where u and v indicate synoptic-scale zonal and meridional winds, respectively, and ϕ is latitude. The overbar denotes the midsummer average from July 1 to August 31. The synoptic eddy fields are retained by applying a bandpass Lanczos filter to the raw daily fields on a 2 – 7 day timescale (Murakami 1979).

The common time period for this study is 1961–2016. Midsummer refers to the mean for July and August. Regression and correlation analyses are employed to investigate the atmospheric circulation anomalies associated with the Arctic sea ice area and rainfall. Student's *t*-test was used to determine statistical significance. Additionally, linear trends are eliminated from all data before analysis to isolate the interannual variation, except in the linear trend calculation of the Arctic sea ice area.

3. Results

3.1 Strengthened relationship between Arctic sea ice and rainfall

The Arctic sea ice area reaches its maximum in March and minimum in September, and has declined substantially during June to November (Parkinson et al. 1999; Dai et al. 2019). Most of Arctic sea ice displays a profound diminishing trend in midsummer during the past 56 years, along with a larger reduction at the marginal seas of the Arctic Ocean, especially over the Beaufort Sea, East Siberian Sea, Laptev Sea, Kara Sea, Greenland Sea and Baffin Bay (Fig. 1c). Moreover, the interannual variability of sea ice is also larger at these regions than other portions (Fig. 1b), which may have an intensified impact on the midlatitude atmospheric circulation and climate variability. The correlation coefficients between the Arctic sea ice area with the PC1 are calculated to identify the region of interest (Fig. 1d). A significant positive correlation can be seen over East Siberian Sea, implying that East Siberian Sea is a key region where the sea ice area is closely related to midsummer rainfall in NEC. Accordingly, a sea ice area index (SIAI) is defined as the normalized area-weighted average of the sea ice area in East Siberian Sea (69 – 74°N, 160 – 190°E; as shown in Fig. 1d).

The connection between the SIAI and PC1 indices is significant during 1961 – 2016 (Fig. 2a), with a correlation coefficient 0.39 (above the 99% confidence level). To detect the potential instability in their relationship, Fig. 2b depicts the 21-year-sliding correlation coefficients between the indices PC1 and SIAI. Insignificant positive correlation coefficients are observed before the mid-1980s. However, positive correlations intensify and become significant after the late 1980s. When the sliding window width changes to 19 and 23 years, this intensified connection is also apparent (figures not shown). To explore the decadal change in the interannual relationship between the SIAI and NEC's rainfall, we selected two

periods based on Figs. 2a and b: 1961 – 1983 (P1) and 1994 – 2016 (P2), each period consisting of 23 years. The middle transitional ten years has been removed. The correlation coefficients are 0.18 (insignificant) during P1 and 0.57 (exceeding the 99% confidence interval) P2, respectively. The spatial distributions of correlation coefficients between the Arctic sea ice area and the PC1 index for the two periods are illustrated in Figs. 2c and d. During P1, positive correlations appear over eastern East Siberian Sea, and negative correlations occupy the Pacific sector of the Arctic Ocean. By comparison, during P2, the positive correlations expand westward over East Siberian Sea. Meanwhile, the negative correlations disappear over the Pacific side of the Arctic and occur at the Franz Josef Land. Given the sea ice displays a relative large declining trend and interannual variability over the East Siberian Sea, this study focused on the relationship between the East Siberian sea ice and NEC's rainfall. Moreover, we also examined the rainfall anomalies associated with the SIAI for two periods. During P1, corresponding to increased sea ice area anomalies in East Siberian Sea, the rainfall anomalies are hardly significant over most of NEC (Fig. 2e); however, predominant positive rainfall anomalies prevail over NEC during P2, especially in the southern part (Fig. 2e). These results confirm that the strengthened relationship between rainfall over NEC and sea ice area in East Siberian Sea is robust.

3.2 Changes in associated atmospheric circulation anomalies

To understand the intensified relationship between the sea ice area in East Siberian Sea and rainfall in NEC after the 1990s, we examine the associated atmospheric circulation anomalies in this section. As shown in Fig. 3, the SIAI□related circulation anomalies have a barotropic structure before and after the 1990s. A positive SIAI is characterized by negative height anomalies and intensified westerly over the Arctic and positive height anomalies over the midlatitudes, with an anomalous anticyclone centered over the North Pacific. By comparison, the regimes are quantitatively larger and spatially broader during P2 than P1. To be specific, the negative SLP geopotential height anomalies strengthen and expand over the whole Arctic during P2, whereas relative weak negative values just appear over the Bering Sea during P1. It is notable that the significant positive SLP and height anomalies are also stronger during P2 and P1. Concurrently, the anticyclone over the midlatitudes dramatically enhances during P2, and elongates westward over the Central North Pacific and East Asia. Han et al. (2020) has revealed that the regime over the Central North Pacific is closely linked with NEC's midsummer rainfall during the whole period. Therefore, it is speculated that the westward elongation and strengthening of the anticyclone over the Central North Pacific associated with a positive SIAI may contribute to a significant SIAI-rainfall relationship after the 1990s.

Moisture conditions and convective activities are critical for rainfall processes, which are determined by atmospheric circulation. Thus, the moisture transport and vertical movement anomalies in association with the SIAI are explored in Fig. 4. During P1, in response to a positive SIAI, the anomalous northwesterly at the west flank of the cyclone centered over the Lake Baikal transports moisture from the inland across the western boundary of NEC (Fig. 4a), which plays a secondary role in rainfall events (Han et al. 2019).

Moreover, weak descending motion anomaly occupies NEC (Fig. 4c), consistent with weak circulation anomalies over East China-West Pacific region (Fig. 3). These regimes induce weak rainfall anomalies at NEC (Fig. 2e). During P2, significant anomalous divergence of moisture dominates the western-central North Pacific (Fig. 4b), which is consistent with the westward elongation of the anticyclone centered over the Central North Pacific (Figs. 3b, d and f). The easterly flow at the southern flank elongates westward and then turns northward, crossing the southern boundary of NEC and causing prominent convergent moisture anomalies. In addition, the anticyclone elongating from the Central North Pacific to Northeast China leads to upper-level divergence and low-level convergence anomalies (FIG. S4), exciting ascending movement anomalies in situ (Fig. 4d). These circulation anomalies jointly facilitate rainfall at NEC (Fig. 2f).

The above results indicate that the North Pacific anticyclone in association with the positive SIAI strengthens and elongate westward over the Central North Pacific after the 1990s, contributing to a significant SIAI-NEC's rainfall relationship via modulating moisture transport and vertical motion. The above result prompts interest in the reasons for the strengthening of the SIAI-related circulation anomalies, which will be explored in the next section.

3.3 Possible mechanism

3.3.1 The effect of increased interannual variability of sea ice

Above analyses suggest that the relationship between sea ice at the East Siberian Sea and NEC's precipitation has strengthened after the 1990s. An accompanied issue to be addressed is: what is the possible factor contributing to this interdecadal change? Chen et al. (2019) have demonstrated that the interannual variability of the Arctic sea ice becomes enlarged after the 1990s, which could induce larger amplitudes of sea ice anomalies as well as heat fluxes and contribute to a stronger Arctic sea ice-Arctic oscillation connection. Motivated by their work, we have compared the sea ice, upward longwave radiation (LWR), surface sensible heat flux (SHF) and surface latent heat flux (LHF) anomalies associated with the SIAI during the two periods.

To facilitate the analysis, the SIAI is multiplied by minus one. Figures 5a1 and a2 exhibits SIA anomalies regressed on the minus one SIAI during 1961 – 1983 and 1994 – 2016, respectively. A negative SIAI index is related to predominant sea ice loss anomalies at the East Siberian Sea during the two periods. By comparison, the amplitude of SIA loss is larger during P2 than during P1 (Fig. 5a3). Previous studies have documented that the Arctic sea ice can lead to air temperature anomalies at the Arctic through modulating LWR, SHF, and LHF (Dai et al. 2019). It is speculated that larger sea ice loss may lead to stronger exchange of heat flux between ocean and atmosphere. Therefore, the surface heat fluxes anomalies in association with the SIAI are examined, including surface LWR, SHF and LHF. As shown in Fig. 5, the declined sea ice is accompanied by increased LWR and SHF released to atmosphere and reduced LHF over East Siberian Sea, with larger anomalies of LWR, SHF and LHF during 1994 – 2016 than

1961 – 1983. Furthermore, Fig. 6 presents the anomalies of LWR, SHF, LHF, and net surface HF (the sum of LWR, SHF and LHF) over East Siberian Sea obtained by regression upon the minus one SIAI for both periods. Consistent with larger sea ice loss during the latter period, the anomalous surface net surface HF that is released from ocean to atmosphere increases from 2.05 W m^{-2} during 1961 – 1983 to 5.01 W m^{-2} during 1994 – 2016, which is attributed to the increases in LWR (from 3.35 W m^{-2} during 1961 – 1983 to 4.63 W m^{-2} during 1994 – 2016) and SHF (from 1.10 W m^{-2} during 1961 – 1983 to 3.04 W m^{-2} during 1994 – 2016).

The amplitude of the net surface HF associated with SIAI decrease in the later period is approximately 2.5 times larger than that during the former period. Correspondingly, the SIAI could induce stronger air temperature anomalies during P2 than during P1 (Fig. S5), leading to stronger meridional temperature gradient after the 1990s. To be Specific, during P2, a negative SIAI index is associated with decreased equator-to-pole temperature gradient at the region between 50°N and 70°N, and increased temperature gradient at the region between 30°N and 45°N (Figs. 7b, d and f). Therefore, the westerly anomalies decelerate at the midlatitudes of North Pacific. However, the temperature gradient and zonal wind anomalies associated with the SIAI are confined over the Northeast Pacific, with weak anomalies at the western-central North Pacific (Figs. 7a, c and e).

The temperature gradient anomalies are related to baroclinicity and may have an influence on eddy activities (Chen et al. 2018). It is speculated that the sea ice at the East Siberian Sea may be associated with the wave-mean flow interaction. Moreover, the interaction between synoptic-scale eddies and mean flow could be qualitatively diagnosed by the extended EP flux. Previous study has demonstrated that the convergences (divergences) of the extended EP flux are accompanied by forcing of anticyclonic (cyclonic) circulation to its north and cyclonic (anticyclonic) circulation to its south (Lau 1988; Chen et al. 2018). Figure 8 shows the anomalies of midsummer extended EP flux at 300 hPa and the corresponding divergence in association with the minus one SIAI during both periods. In response to a negative SIAI, significant convergence anomalies of the extended EP flux appears over the high latitudes of the North Pacific as well as over NEC and divergence anomalies occur over the midlatitudes during 1994 – 2016 (Fig. 8b), which are accompanied by easterly (westerly) wind anomalies at approximately 50 – 60°N (30 – 45°N) (Fig. 7d). Accordingly, a strong cyclonic vorticity forcing appears to the north of divergence region and south of the convergence region, i.e., approximately 40 – 50°N, and that an anticyclonic vorticity forcing appears south of the divergence region, i.e., approximately 25 – 35°N, and north of the convergence region, i.e., north of 60°N (Fig. 8d). These explain the development of the positive height and anticyclonic anomalies over the western-central North Pacific (Figs. 3b, d and f). In contrast, the anomalous divergence and convergence of the extended EP flux and vorticity forcing are relative weak over East Asia and the North Pacific during 1961 – 1983, consistent with weak westerly wind at high latitudes and easterly wind at midlatitudes of the Northeast Pacific. It explains the appearance of relatively weak geopotential height and horizontal wind anomalies over the North Pacific during the former period (Figs. 3a, c and e).

The larger amplitude of sea ice area anomalies in East Siberian Sea is associated with enlarged interannual variability after the 1990s. As shown in Fig. 9a, the interannual variability is greater over northern East Siberian Sea during the latter period than the former period. Figure 9b depicts the 21-year sliding standard deviation of the sea ice area at East Siberian Sea. It is obvious that the interannual variability is larger after the mid-1980s. It suggests that the larger amplitude of the East Siberian sea ice anomalies due to an enlarged interannual variability have an strengthened connection with temperature gradient anomalies and the interaction between synoptic-scale eddies and mean flow at the western-central North Pacific. This indicates that the change in the sea ice area in East Siberian Sea is a likely contributor to the enhanced connection between the SIAI and circulation anomalies over the North Pacific.

3.2 The western elongation of background circulation at the Central North Pacific

It is notable that the anticyclone associated with the SIAI elongates westward after the 1990s, which is centered over the Northeast Pacific during P1 and is centered over the Central North Pacific during P2 (Fig. 3). The western elongation of the anticyclone facilitates the prevalence of significant moisture divergence anomalies centered at the western-central North Pacific (Fig. 4b). The southerly flow at the western flank of the moisture divergence transports water vapor deriving from the subtropical West Pacific to NEC across the southern boundary. However, the anticyclone and moisture divergence anomalies associated with the SIAI are confined over the Northeast Pacific during P1, which has an insignificant influence on NEC's precipitation.

We speculated that the westward elongation of the anticyclone may be related with the change in the background circulation over the North Pacific. The EOF analysis is performed for midsummer SLP over the midlatitude North Pacific (30º–55ºN, 120ºE–120ºW) during the two periods. The first EOF mode features homogeneous SLP anomalies over the North Pacific (Fig. 10). During P1, the EOF1 mode is centered over the Northeast Pacific, and the main body is located in the east of dateline; by contrast, the EOF1 mode elongates westward remarkably and is centered at the central North Pacific during P2. The westward extension of the EOF1 mode is consistent with the western elongation of the anticyclone at the Central North Pacific in association with a positive SIAI.

To characterize the structural change of the background circulation over the North Pacific in detail, we calculate the first EOF of the North Pacific SLP during each of 36 overlapping 21 years. The central year is 1971 for the period 1961–1981, for example. The figures are shown every four years for brevity. The center of the SLP at the North Pacific locates east of 160°W before the late 1980s; however, the center shifts westwards and locates west of the date line after the 1990s (Fig. 11). Moreover, it should be noted that the western extension of the circulation over the North Pacific can also be obtained based on the fifth-generation ECMWF atmospheric reanalysis dataset (Figs. S6 and S7). It suggests that the western elongation of the circulation over the North Pacific is robust. Therefore, the main body of the background

circulation at the North Pacific shifts from the Northeast Pacific to the central North Pacific after the 1990s, which may contribute to the westward elongation of the SIAI-circulation at the North Pacific.

4. Conclusion

This study documents a strengthened relationship between sea ice area over East Siberian Sea and midsummer rainfall at NEC after the 1990s. The relationship between the SIAI and NEC's rainfall is insignificant during the period 1961 – 1983 and becomes significantly positive during 1994 – 2016. During the latter period, the anticyclone over the Central North Pacific associated with the SIAI becomes strengthened and elongates westward, which further affects NEC's rainfall through modulating moisture transport and vertical movement.

In addition, the change in interannual variability in East Siberian sea ice is a likely factor contributing to the enhanced connection between the SIAI and circulation anomalies at the midlatitudes. The amplitude of sea ice anomalies is larger during 1994 – 2016 than during 1961 – 1983 due to an enlarged interannual variability. Consistently, the SIAI-related surface heat fluxes anomalies are stronger during 1994 – 2016 than 1961 – 1983, which further induces stronger meridional temperature gradient anomalies and strengthened interaction between synoptic-scale eddies and mean flow. Therefore, the circulation anomalies related to the SIAI intensified over the North Pacific. Moreover, the background circulation at the North Pacific shifts from the Northeast Pacific to the Central North Pacific, facilitating the western elongation of the SIAI-related anticyclone over the Central North Pacific. These conditions jointly contribute to strengthened circulation anomalies at the midlatitudes in association with the SIAI (Fig. 12). Thus, the positive connection between the SIAI and the rainfall at NEC is established after the 1990s.

Declarations

Acknowledgments

This work was jointly supported by Guangdong Major Project of Basic and Applied Basic Research (Grant No. 2020B0301030004) and the National Natural Science Foundation of China (Grants Nos. 42025502, 41875118 and 41875119).

References

1. Balmaseda MA, Ferranti L, Moteni F, Palmer TN (2010) Impact of 2007 and 2008 Arctic ice anomalies on the atmospheric circulation: implications for long-range predictions. Q J R Meteor Soc 136:1655–1664. https://doi.org/10.1002/qj.661
2. Bhatt US, Alexander MA, Deser C, Walsh JE, Walsh JS, Miller JS, Timlin MS, Scott J, Tomas RA (2008) : The Atmospheric Response to Realistic Reduced Summer Arctic Sea Ice Anomalies. In Arctic sea ice decline: observations, projections, mechanisms, and implications. In: DeWeaver ET, Bitz CM, Tremblay LB (eds) Geophyical. Monogaph. Series, 180: 91–110. AGU: Washington, DC

3. Blackport R, Screen JA, van der Wiel K, Bintanja R (2019) Minimal influence of reduced Arctic sea ice on coincident cold winters in mid-latitudes. Nat Clim Change 9:697–704. doi: 10.1038/s41558-019-0551-4
4. Cai M, Yang S, Van Den Dool HM, Kousky VE (2007) : Dynamical implications of the orientation of atmospheric eddies: a local energetics perspective. *Tellus*, **59** A, 127–140, https://doi.org/10.1111/j.1600-0870.2006.00213.x
5. Chen SF, Ren RG, Chen W (2018) A strengthened impact of November Arctic oscillation on subsequent tropical Pacific sea surface temperature variation since the late-1970s. Clim Dyn 51:511–529. doi: 10.1007/s00382-017-3937-x
6. Chen SF, Ren RG, Chen W (2019) Enhanced impact of Arctic sea ice change during boreal autumn on the following spring Arctic oscillation since the mid-1990s. Clim Dyn 53:5607–5621. doi: 10.1007/s00382-019-04886-y
7. Cohen J, Coauthors (2020) Divergent consensuses on Arctic amplification influence on midlatitude severe winter weather. Nat Clim Chang 10:20–29. https://doi.org/10.1038/s41558-019-0662-y
8. Dai AG, Luo DH, Song MR, Liu JP (2019) Arctic amplifcation is caused by sea-ice loss under increasing CO2. Nat Commun 10:121. https://doi.org/10.1038/s41467-018-07954-9
9. Dethloff K, Coauthors (2006) A dynamical link between the Arctic and the global climate system. Geophys Res Lett 33:L03703. https://doi.org/10.1029/2005GL025245
10. Francis JA, Skific N, Vavrus SJ (2020) Increased persistence of large-scale circulation regimes over Asia in the era of amplified Arctic warming, past and future. Sci Rep 10:1–13. https://doi.org/10.1038/s41598-020-71945-4
11. Frankignoul C, Sennécheal N (2007) Observed Influence of North Pacific SST Anomalies on the Atmospheric Circulation. J Clim 20:592–606. https://doi.org/10.1175/JCLI4021.1
12. Gao ZT, Hu ZZ, Jha B, Yang S, Zhu JS, Shen BZ, Zhang RJ (2014a) Variability and predictability of Northeast China climate during 1948–2012. Clim Dyn 43:787–804. https://doi.org/10.1007/s00382-013-1944-0
13. —, — JS, Zhu S, Yang RH, Zhang ZN, Xiao, Jha B (2014b) Variability of Summer Rainfall in Northeast China and Its Connection with Spring Rainfall Variability in the Huang-Huai Region and Indian Ocean SST. J Clim 27:7086–7101. https://doi.org/10.1175/JCLI-D-14-00217.1
14. Gao YQ, Coauthors (2015) Arctic sea ice and Eurasian climate: A review. Adv Atmos Sci 32:92–114. https://doi.org/10.1007/s00376-014-0009-6
15. Guo D, Coauthors (2014) Mechanism on how the spring Arctic sea ice impacts the East Asian summer monsoon. Theor App l Climatol 115:107–119. https://doi.org/10.1007/s00704-013-0872-6
16. Han TT, Chen HP, Wang HJ (2015) Recent changes in summer precipitation in Northeast China and the background circulation. Int J Climatol 35:4210–4219. https://doi.org/10.1002/joc.4280
17. — SP, He HJ, Wang, Hao X (2018) Enhanced influence of early-spring tropical Indian Ocean SST on the following early-summer precipitation over Northeast China. Clim Dyn 51:4065–4076. https://doi.org/10.1007/s00382-017-3669-y

18. — —, —, and — (2019) Variation in principal modes of midsummer precipitation over Northeast China and its associated atmospheric circulation. Adv Atmos Sci 36:55–64. https://doi.org/10.1007/s00376-018-8072-z
19. — HJ, Wang, Sun JQ (2017) Strengthened relationship between eastern ENSO and summer precipitation over Northeastern China. J Clim 30:4497–4512. https://doi.org/10.1175/JCLI-D-16-0551.1
20. — MH, Zhang BT, Zhou X, Hao, Li SF (2020) Strengthened relationship between tropical West Pacific and midsummer precipitation over Northeast China after the mid-1990s. J Clim 33:6833–6848. https://doi.org/10.1175/JCLI-D-19-0957.1
21. Honda M, Inoue J, Yamane S (2009) Influence of low Arctic sea ice minima on anomalously cold Eurasian winters. Geophys Res Lett 36:L08707. https://doi.org/10.1029/2008GL037079
22. Jin FF, Pan LL, Watanabe M (2006) Dynamics of Synoptic Eddy and Low-Frequency Flow Interaction. Part I: A Linear Closure. J Atmos Sci 63:1677–1694. doi: https://doi.org/10.1175/JAS3715.1
23. Li HX, Chen HP, Wang HJ, Sun JQ, Ma JH (2018) Can Barents Sea Ice Decline in Spring Enhance Summer Hot Drought Events over Northeastern China? J Clim 31:4705–4725. https://doi.org/10.1175/JCLI-D-17-0429.1
24. Li S, Ding ZY, Dai P, Liu YH, Han Y (2016) Recent Advances in Rearch on Northeast China. J Arid Meteorol 34:13–19. doi:10.11755/j.issn.1006-7639(2016)-01-0013
25. Liang LQ, Li LJ, Liu Q (2011) Precipitation variability in Northeast China from 1961 to 2008. J Hydr 404:67–76. https://doi.org/10.1016/j.jhydrol.2011.04.020
26. Liu JP, Curry JA, Wang HJ, Song MR, Horton RM (2012) Impact of declining Arctic sea ice on winter snowfall. P N A Sci 109:4074–4079. https://doi.org/10.1073/pnas.1114910109
27. Liu Y, Zhu YL, Wang HJ, Yong YQ, Sun JQ, Wang T, Ma JH, Yurova A, Li F (2020) Role of autumn Arctic Sea ice in the subsequent summer precipitation variability over East Asia. Int J Climatol 40:706–722. https://doi.org/10.1002/joc.6232
28. Luo DH, Chen XD, Overland J, Simmonds I, Wu YT, Zhang PF (2019) Weakened potential vorticity barrier linked to recent winter Arctic sea ice loss and midlatitude cold extremes. J Clim 32:4235–4261. doi: 10.1175/JCLI-D-18-0449.1
29. Mori M, Watanabe M, Shiogama H, Inoue J, Kimoto M (2014) Robust Arctic sea-ice influence on the frequent Eurasian cold winters in past decades. Nat Geosci 7:869–873. https://doi.org/10.1038/ngeo2277
30. Ogawa F, and Co-authors (2018) Evaluating impacts of recent Arctic sea ice loss on the northern hemisphere winter climate change. Geophys Res Lett 47:3255–3263. doi: 10.1002/2017GL076502
31. Parkinson CL, Cavalieri DJ, Gloersen P, Zwally HJ, Comiso JC (1999) Arctic sea ice extents, areas and trends, 1978 – 1996. J Geophys Res 104:20837–20856. https://doi.org/10.1029/1999JC900082
32. Petrie RE, Shaffrey LC, Sutton RT (2015) Atmospheric response in summer linked to recent Arctic sea ice loss. Q J R Meteorol Soc 141:2070–2076. doi: 10.1002/qj.2502

33. Rayner NA, Coauthors (2003) Global analyses of sea surface temperature, sea ice, and night marine air temperature since the late nineteenth century. J Geophys Res 108:4407. doi: 10.1029/2002JD002670
34. Screen JA (2013) Influence of Arctic sea ice on European summer precipitation. Environ Res Lett 8:044015. doi: 10.1088/1748-9326/8/4/044015
35. Screen JA, Francis JA (2016) Contribution of sea ice loss to Arctic amplification is regulated by Pacific Ocean decadal variability. Nat Clim Change 6:856–860. https://doi.org/10.1038/nclimate3011
36. Screen JA, Coauthors (2018) Consistency and discrepancy in the atmospheric response to Arctic sea-ice loss across climate models. Nat Geo 11:155–163. https://doi.org/10.1038/s41561-018-0059-y
37. Shen BZ, Lin ZD, Lu RY, Lian Y (2011) Circulation anomalies associated with interannual variation of early- and late-summer precipitation in Northeast China. Sci China Earth Sci 54:1095–1104. https://doi.org/10.1007/s11430-011-4173-6
38. Sun L, An G, Ding L, Shen BZ (2000) A climatic analysis of summer precipitation features and anomaly in Northeast China. Acta Meteor Sinica 58:70–82
39. — BZ, Shen B, Sui, Huang BH (2017) The influences of East Asian summer monsoon on summer precipitation in Northeast China. Clim Dyn 48:1657–1659. https://doi.org/10.1007/ s00382-016-3165-9
40. Tang QH, Zhang XJ, Yang XH, Francis JA (2013) Cold winter extremes in northern continents linked to Arctic sea ice loss. Environ Res Lett 8:014036. doi:10.1088/1748-9326/8/1/014036
41. Vihma T (2014) Effects of Arctic sea ice decline on weather and climate: A review. Surv Geophys 35:1175–1214. https://doi.org/10.1007/s10712-014-9284-0
42. Wang HJ, He SP (2015) The North China/Northeastern Asia Severe Summer Drought in 2014. J Clim 28:6667–6681. https://doi.org/10.1175/JCLI-D-15-0202.1
43. Wu BY, Zhang RH, Wang B, D'Arrigo R (2009) On the association between spring Arctic sea ice concentration and Chinese summer rainfall. Geophys Res Lett 36:L09501. https://doi.org/10.1029/2009GL037299
44. Wu J, Gao XJ (2013) A gridded daily observation dataset over China region and comparison with the other datasets. Chin J Geophys 56:1102–1111
45. Zhou MZ, Wang HJ (2015) Potential impact of future climate change on crop yield in northeastern China. Adv Atmos Sci 32(7):889–897. doi: 10.1007/s00376-014-4161-9
46. Zhou MZ, Wang HJ (2014) Late Winter Sea Ice in the Bering Sea Predictor for Maize and Rice Production in Northeast China. J Appl Meteor Climatol 53:1183–1192. https://doi.org/10.1175/JAMC-D-13-0242.1
47. Zhou MZ, Wang HJ, Yang S, K. and Fan (2013) Influence of springtime North Atlantic Oscillation on crops yields in Northeast China. Clim Dyn 41:3317–3324. https://doi.org/10.1007/s00382-012-1597-4

48. Zhu YL (2011) A seasonal prediction model for the summer rainfall in northeast China using the year-to-year increment approach. Atmos Ocean Sci Lett 4:146–150. https://doi.org/10.1080/16742834.2011.11446920
49. Zuo H, C SH, Lu, Hu YQ (2004) : Variation trend of yearly mean air temperature and precipitation in China in the last 50 years. *Plateau Meteor.*, **23**, 238–244, https://doi.org/1000-0534(2004)02-0238-07
50. Zappa G, Pithan F, Shepherd TG (2018) Multi-model evidence for an atmospheric circulation response to Arctic sea ice loss in the CMIP5 future projections. Geophys Res Lett 45:1011–1019. doi: 10.1002/2017GL076096
51. Wu, J., and X. J. Gao, 2013: A gridded daily observation dataset over China region and comparison with the other datasets. *Chin. J. Geophys.*, **56**, 1102–1111.
52. Zhang, Y., J. M. Wallace, and N. Iwasaka, 1996: Is Climate Variability over the North Pacific a Linear Response to ENSO? *J. Climate*, **9**, 1468–1478, https://doi.org/10.1175/1520-0442(1996)009<1468:ICVOTN>2.0.CO;2.
53. Zhao, P., X. D. Zhang, X. J. Zhou, M. Ikeda, and Y. H. Yin, 2004: The sea ice extent anomaly in the North Pacific and its Impact on the East Asian summer monsoon rainfall. *J. Climate*, **17**, 3434–3447, https://doi.org/10.1175/1520-0442(2004)017<3434:TSIEAI>2.0.CO;2.
54. Zhou, M. Z., and H. J. Wang, 2015: Potential impact of future climate change on crop yield in northeastern China. Adv. Atmos. Sci., 32(7), 889–897, doi: 10.1007/s00376-014-4161-9.
55. Zhou, M. Z., H. J. Wang 2014: Late Winter Sea Ice in the Bering Sea Predictor for Maize and Rice Production in Northeast China. *J. Appl. Meteor. Climatol.*, **53**, 1183–1192, https://doi.org/10.1175/JAMC-D-13-0242.1.
56. Zhou, M. Z., H. J. Wang, S. Yang, K. and Fan, 2013: Influence of springtime North Atlantic Oscillation on crops yields in Northeast China. *Climate Dyn.*, **41**, 3317–3324, https://doi.org/10.1007/s00382-012-1597-4.
57. Zhu, Y. L., 2011: A seasonal prediction model for the summer rainfall in northeast China using the year-to-year increment approach. *Atmos. Oceanic Sci. Lett.*, **4**, 146–150, https://doi.org/10.1080/16742834.2011.11446920.
58. Zuo, H. C, S. H. Lu, and Y. Q. Hu, 2004: Variation trend of yearly mean air temperature and precipitation in China in the last 50 years. *Plateau Meteor.*, **23**, 238–244, https://doi.org/1000-0534(2004)02-0238-07.
59. Zappa, G., F. Pithan, and T. G. Shepherd, 2018: Multi-model evidence for an atmospheric circulation response to Arctic sea ice loss in the CMIP5 future projections. *Geophys. Res. Lett.*, **45**, 1011–1019, doi: 10.1002/2017GL076096.

Figures

Figure 1

a Linear regression of rainfall (mm) against the normalized first principal component (PC1) of the EOF1 mode of midsummer rainfall over Northeast China (NEC) for 1961–2016. **b** Standard deviation (10^2 km^2) of midsummer Arctic sea ice area (SIA) north of 65ºN for the period 1961–2016. **c** Linear trend (10^2 km^2 per year) of midsummer Arctic SIA north of 65ºN during 1961–2016. **d** Correlation map between midsummer Arctic SIA and the PC1 index. Stippling areas in **a**, **c** and **d** indicate the values that significantly exceed the 95% confidence level, estimated using Student's *t*-test. The rectangular area in **b** and **d** represents the selected region for the SIA index at East Siberian Sea (69º–74ºN, 160º–190ºE; SIAI).

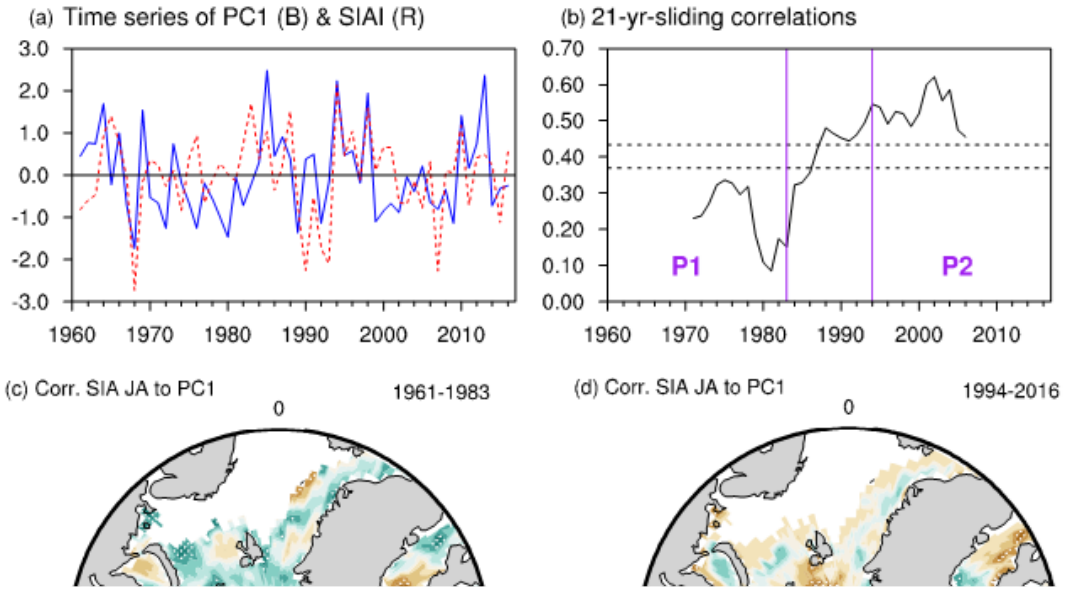

Figure 2

a Time series of the PC1 (blue line) and SIAI index (red line) during 1961–2016 and **b** the 21-year sliding correlation coefficients between the two indices. Horizontal broken line donates the 90% confidence level, based on Student's *t*-test. The two vertical lines represent the years 1983 and 1994, respectively. Correlation coefficients of midsummer Arctic SIA and the PC1 index during **c** 1961–1983 and **d** 1994–2016. Linear regression pattern of midsummer rainfall (mm) against the SIAI for **e** 1961–1983 and **f**

1994–2016. Stippling areas in **e–f** indicate the values that significantly exceed the 90% confidence level, estimated using Student's *t*-test.

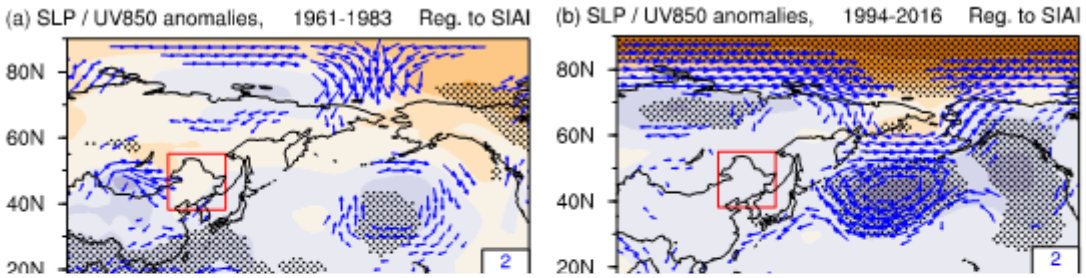

Figure 3

Linear regression pattern of midsummer **a**, **b** SLP (mb) and 850-hPa horizontal wind (m s^{-1}), **c**, **d** 500-hPa geopotential height (m) and horizontal wind (m s^{-1}), **e**, **f** 300-hPa geopotential height (m) and horizontal wind (m s^{-1}) against the SIAI for 1961–1983 (left panels) and 1994–2016 (right panels). Stippling areas indicate the values that significantly exceed the 90% confidence level, estimated using Student's *t*-test. Vectors exceeding the 90% confidence level are plotted.

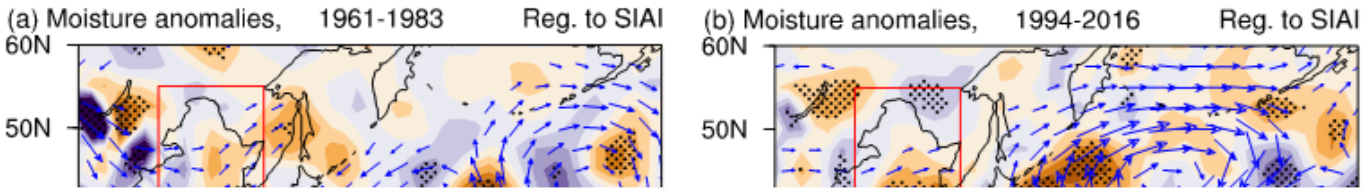

Figure 4

Linear regression pattern of midsummer **a**, **b** vertically integrated moisture flux from the surface to 300 hPa (vectors, kg m^{-1} s^{-1}) and its divergence (shadings, 10^{-6} kg s^{-1}), and **c**, **d** 500-hPa vertical movement (Pa s^{-1}) against the SIAI for 1961–1983 (left panels) and 1994–2016 (right panels). Stippling areas indicate the values that significantly exceed the 90% confidence level, estimated using Student's *t*-test. Vectors in **a–b** greater than 10 (kg m^{-1} s^{-1}) are plotted. Dark (light) shadings in **c–d** indicate the 95% (90%) confidence level, estimated using Student's *t*-test.

Figure 5

Linear regression pattern of midsummer **a1**, **a2** sea ice area (10^2 km^2), **b1**, **b2** upward longwave radiation (LWR; W m^{-2}), **c1**, **c2** surface sensible net heat flux (SHF; W m^{-2}), and **d1**, **d2** surface latent net heat flux (LHF; W m^{-2}) against the minus one SIAI for 1961–1983 (left panels) and 1994–2016 (middle panels). Changes of **a3** SIA, **b3** LWR (W m^{-2}), **c3** SHF (W m^{-2}), and **d3** LHF (W m^{-2}) anomalies between 1994–

2016 and 1961–1983, obtained by the middle column minus the left column. Stippling (crossing) areas indicate the values that significantly exceed the 95% (90%) confidence level, estimated using Student's *t*-test.

Figure 6

Regional mean LWR, SHF, and LHF anomalies (W m^{-2}) and net surface heat flux (HF; W m^{-2}) over East Siberian Sea obtained by regression upon the minus one SIAI index during 1961–1983 (red bars) and 1994–2016 (blue bars). Positive values indicate upward direction.

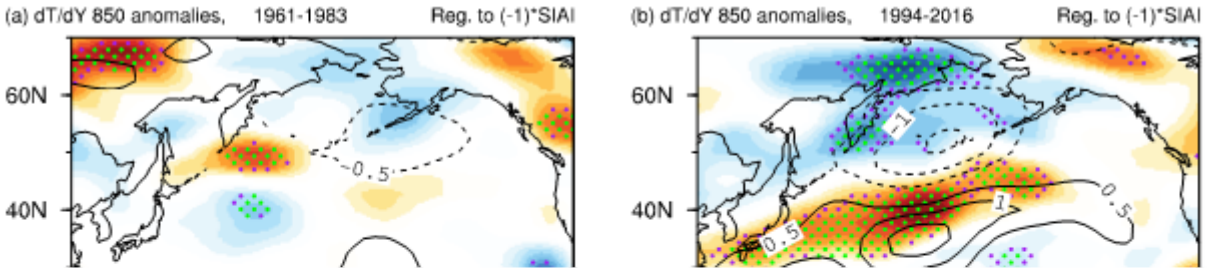

Figure 7

Linear regression pattern of midsummer equator-to-pole air temperature gradient (shadings; right panel) and zonal wind (contours) against the minus one SIAI for 1994–2016 at **a** 850 hPa, **b** 500 hPa and **c** 300 hPa. Green (purple) stippling areas indicate that the equator-to-pole temperature gradient anomalies significantly exceed the 95% (90%) confidence level, estimated using Student's *t*-test.

Figure 8

Linear regression pattern of midsummer **a**, **b** 300-hPa zonal wind (contours, m s^{-1}), extended EP flux (vectors, m^2 s^{-2}) and its divergence (shadings, 10^{-5} m s^{-2}), and **c**, **d** 300-hPa vorticity (contours, 10^{-6} s^{-1}) and divergence wind components (vectors, m s^{-1}) with regard to the minus one SIAI for 1961–1983 (left panels) and 1994–2016 (right panels). Vectors exceeding the 90% confidence level are plotted. Dark (light) shading in **c**, **d** indicates values that significantly exceed the 95% (90%) confidence level, estimated using the Student's *t*-test.

Figure 9

a The differences in standard deviation of the sea ice area (10^2 km^2) over the East Siberian Sea between 1994–2016 and 1961–1983. **b** The time series of interannual variability (10^2 km^2) of the East Siberian Sea SIA during 1961–2016. The interannual variability of defined as the 21-year moving standard deviation of the SIA averaged at East Siberian Sea during 1961–2016. The horizontal line indicate the interannual variability 5×10^2 km^2.

Figure 10

The leading EOF mode of midsummer SLP over the North Pacific (30°–55°N, 120°E–120°W) during **a** 1961–1983 and **b** 1994–2016. The number in the upper right corner indicates the explained variance.

Figure 11

Same as **Fig. 10**, except for a 21-year-sliding window. The year of each panel indicates the central year of the sliding window. The figure is shown every four years for brevity.

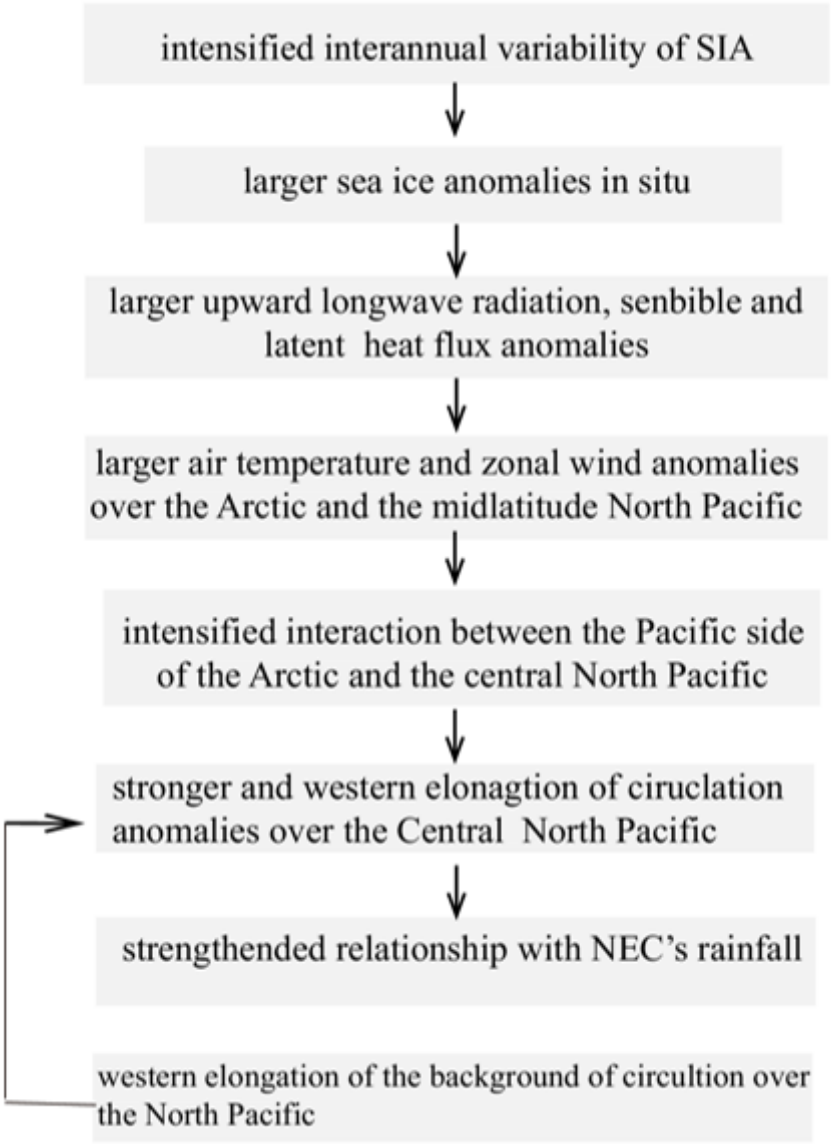

Figure 12

Same as **Fig. 10**, except for a 21-year-sliding window. The year of each panel indicates the central year of the sliding window. The figure is shown every four years for brevity.

Supplementary Files

This is a list of supplementary files associated with this preprint. Click to download.

- supplementary.docx